Subgrid-scale stresses and scalar fluxes constructed by the multi-scale turnover Lagrangian map

Sukaina AL-Bairmani,[1] Yi Li,[1, a)] Carlos Rosales,[2] and Zheng-tong Xie[3]
[1)] *School of Mathematics and Statistics, University of Sheffield, Sheffield, UK, S3 7RH*
[2)] *Department of Mechanical Engineering, Universidad Tecnica Federico Santa Maria, Valparaiso, Chile*
[3)] *Engineering and Environment, University of Southampton, Southampton, UK, SO17 1BJ*

(Dated: 27 February 2017)

The multi-scale turnover Lagrangian map (MTLM) [C. Rosales and C. Meneveau, Phys. Rev. E **78**, 016313 (2008)] uses nested multi-scale Lagrangian advection of fluid particles to distort a Gaussian velocity field and, as a result, generate non-Gaussian synthetic velocity fields. Passive scalar fields can be generated with the procedure when the fluid particles carry a scalar property [C. Rosales, Phys. Fluids **23**, 075106 (2011)]. The synthetic fields have been shown to possess highly realistic statistics characterizing small scale intermittency, geometrical structures and vortex dynamics. In this paper, we present a study of the synthetic fields using the filtering approach. This approach, which has not been pursued so far, provides insights on the potential applications of the synthetic fields in large eddy simulations and subgrid-scale modelling. The MTLM method is first generalized to model scalar fields produced by an imposed linear mean profile. We then calculate the subgrid-scale (SGS) stress, SGS scalar flux, SGS scalar variance, as well as related quantities from the synthetic fields. Comparison with direct numerical simulations (DNS) shows that the synthetic fields reproduce the probability distributions of the SGS energy and scalar dissipation rather well. Related geometrical statistics also display close agreement with DNS results. The synthetic fields slightly under-estimate the mean SGS energy dissipation, and slightly over-predict the mean SGS scalar variance dissipation. In general, the synthetic fields tend to slightly under-estimate the probability of large fluctuations for most quantities we have examined. Small scale anisotropy in the scalar field originated from the imposed mean gradient is captured. The sensitivity of the synthetic fields on the input spectra is assessed by using truncated spectra or model spectra as the input. Analyses show that most of the SGS statistics agree well with those from MTLM fields with DNS spectra as the input. For the mean SGS energy dissipation, some significant deviation is observed. However, it is shown that the deviation can be parametrized by the input energy spectrum, which demonstrates the robustness of the MTLM procedure.

I. INTRODUCTION

The transport and mixing of passive scalars by turbulent flows is a phenomenon of both practical and fundamental interests due to its wide applications[17,18,36]. The subject has attracted continuous interests; to name a few, we note recent efforts that have led to new insights into its scaling properties[37], its role in cloud formation[38], and its modelling.[12] One approach to understand and model the mechanisms of turbulent mixing is to use synthetic turbulence models.[5,6,9,10,19,20,22–26] Synthetic turbulence refers to stochastic fields that have characteristics of real hydrodynamic turbulent flows. This methodology aims to construct the field variables (such as velocity and scalar fields) by simpler processes, while reproducing the remarkable characteristics of turbulent fields. Synthetic fields can be generated with little computational cost. Yet, various synthetic models, with different levels of sophistication, have found a wide range of applications.

Many models have been proposed with the applications in large eddy simulations (LES) in mind. In LES, artificial field data are usually needed to initialize the calculation and/or provide the inflow boundary condition. Synthetic turbulence is one of the main methods used to meet this need[7–11,47,48]. These models have found wide applications in conjunction with LES. Nevertheless, the main aim of these methods has been matching the mean velocity profiles, the second order moments and the integral length scales. No significant effort has been devoted to modelling the nonlinear interactions in real turbulence in an efficient way, even though the latter has been identified as an important factor to make further improvement[48]. In one of the most popular methods, the synthetic eddy method (SEM), the synthetic field is composed of localized velocity fluctuations (the eddies). Arguably, the nonlinear interaction could be captured to some extent, since the eddies are allowed to evolve over a short time. Nevertheless, no systematic research has been reported on this aspect of the method, and results shown in [7] suggest that key nonlinear features of real turbulence are missing in SEM fields. Finally, it is worth noting that, apart from the above applications, synthetic models have also been used directly as a subgrid-scale (SGS) model in some simulations (see, e.g., [39] and [40] and references therein).

[a)] Corresponding author. Email: yili@sheffield.ac.uk.

Other synthetic models have been proposed as a vehicle to study the fundamental mechanisms of real turbulence. For instance, particle dispersion has been studied by means of kinematic simulations[6,41,42], and multifractal models[5,19–21,49,50] have been proposed to understand some aspects of real turbulence, in particular small scale intermittency. However, going beyond Gaussian models, it has proven no easy task to synthetic three-dimensional (3D) velocity fields with realistic statistical and structural characteristics of turbulence. A new procedure based on the multi-scale turnover Lagrangian map (MTLM) is proposed in [1] and [2]. The MTLM procedure builds a velocity field by distorting an initially random field via a non-linear map over a hierarchy of spatial scales. Results show that the procedure allows both the statistical and the structural properties of the velocity field as well as the pressure field in real turbulence are faithfully reproduced[1,2,44].

The MTLM procedure has been generalized to turbulent mixing[14] in the convective-inertial regime[4,18,43], in which the fluid particles carry a passive scalar. The mapping thus also distorts the scalar field recursively in a multi-scale fashion. Results show that the MTLM procedure allows the synthetic velocity field to establish the coherence among the particles transporting the scalar, leading to correct level of decorrelation over separation[14]. Numerical results show that the synthetic scalar fields have stronger intermittency in the dissipative and inertial ranges than its advecting velocity field, as is observed in real turbulent fields. Quantitative agreement was found for high-order statistics, the scaling exponents for structure functions, and the characteristics of the dissipation fields. Finally, the spatial structures of the scalar field are also close to experimental results. As a result, the statistical geometry at dissipative scales that results from the conjunction of velocity and scalar gradients behaves in agreement with a real scalar turbulence[14].

The MTLM method has been used to investigate the closure for the pressure Hessian in the Lagrangian models for the velocity gradient[44], to synthesize magnetic fields[45], and to study particle clustering[46]. Applications to inhomogeneous turbulence have also been explored[3,13]. What is missing is the perspective of subgrid-scale (SGS) modelling. Such a perspective is crucial given the potential applications of the MTLM fields in LES, either as SGS models or as initial/boundary conditions, in particular in the LES of, e.g., particle dispersion in atmospheric boundary layer, particulate flows and combustion. Thus, we present in this paper an *a priori* analysis of the filtered synthetic MTLM velocity and scalar fields, and the corresponding SGS stresses and SGS scalar fluxes. Specifically, we have three objectives. Firstly, to model a more realistic scalar field, we generalize the MTLM to the mixing of a passive scalar with a linear mean profile, following the suggestion in [14]. Secondly, we examine the statistics related to the SGS stresses, the SGS scalar flux, and related quantities. We aim to find out if the synthetic fields are able to capture the SGS energy and scalar dissipation correctly, and if they are able to capture the geometrical statistics of the SGS motions. We also examine if the synthetic scalar field captures the effects of the mean scalar profile, as documented in DNS studies by, e. g., [15]. Thirdly, we note that the MTLM procedure requires the energy spectrum (and, for MTLM with scalar advection, the scalar spectrum) as part of the input. A question is how the synthetic fields depend on the input spectra. We thus also perform analysis of MTLM fields obtained using modified spectra. The results of the above three objectives provide useful insights to the ability and robustness of the MTLM fields to model the SGS stress and flux, and other SGS processes.

In Section II, we explain briefly the advection of a passive scalar by turbulent velocity fields. The proposed MTLM procedure is described in detail in Section III. Section IV reviews the key concepts in LES and SGS modelling. In Section V, we consider the statistics of the filtered MTLM scalar and velocity fields, and those of the SGS stresses and fluxes, where the geometric alignment statistics of real and modelled stress tensors are also examined. The effects of modified spectra are also presented in Section V. Conclusions are summarized in Section VI.

II. THE ADVECTION OF A PASSIVE SCALAR

The mixing of a passive scalar Θ is governed by the linear advection-diffusion equation

$$\partial_t \Theta + (\mathbf{u}\cdot\nabla)\Theta = \kappa\nabla^2\Theta + S(\mathbf{x},t). \tag{1}$$

In the above equation, the passive scalar Θ is mixed by a turbulent velocity field $\mathbf{u}(\mathbf{x},t)$, in the presence of a constant molecular diffusivity κ, and a source term $S(\mathbf{x},t)$. Θ could represent, e.g., the temperature perturbation in a flow field where the buoyancy force can be neglected.

The velocity field $\mathbf{u}$ is governed by the forced Navier-Stokes (NS) equation

$$\partial_t \mathbf{u} + \mathbf{u}\cdot\nabla\mathbf{u} = -\nabla p + \nu\nabla^2\mathbf{u} + \mathbf{f}, \tag{2}$$

and the continuity equation

$$\nabla\cdot\mathbf{u} = 0. \tag{3}$$

In Eq. 2, p is the pressure field, ν is the kinematic viscosity, and $\mathbf{f}$ is the external forcing term. $\rho = 1$ has been assumed.

The scalar field is advected by the velocity field, which squeezes and stretches the former. As a consequence, the characteristic length scale of a parcel of the scalar decreases and a scalar variance cascade is generated, accompanying the turbulent kinetic energy cascade. In the inertial range of homogeneous turbulence, the energy spectrum $E(k)$ is, according to the Kolmogorov phenomenology,

$$E(k) = C_K \langle\epsilon\rangle^{2/3} k^{-5/3}, \tag{4}$$

where $k \equiv |\mathbf{k}|$ is the magnitude of the wavenumber $\mathbf{k}$, and C_K is the Kolmogorov constant. The scalar cascade at a particular length scale is governed by the relevant straining time scale of the velocity field. Depending on the Schmidt number $Sc = \nu/\kappa$, three regimes can be identified[4,43]. We consider only the case where $Sc \sim 1$. In this so-called inertial-convective regime, the dominant straining time scale for the scalar field is the local eddy turnover time scale, and the spectrum of scalar variance $E_\theta(k)$ is given by

$$E_\theta(k) = C_{OC}\langle\epsilon\rangle^{-1/3}\langle\epsilon_\theta\rangle k^{-5/3}, \tag{5}$$

where $\langle\epsilon_\theta\rangle = \kappa\langle|\nabla\theta|^2\rangle$ is the mean dissipation of scalar variance, and C_{OC} is the Obukhov-Corrsin constant.

Scalar fluctuations have to be maintained by a source $S(\mathbf{x}, t)$. In this paper we consider fluctuations generated by a linear mean variation with respect to space. Thus, we may write

$$\Theta(\mathbf{x}, t) = \mathbf{G}\cdot\mathbf{x} + \theta(\mathbf{x}, t), \tag{6}$$

where $\theta(\mathbf{x}, t)$ is the scalar fluctuation, and $\mathbf{G}$ indicates the imposed uniform mean scalar gradient. As a result, the equation for θ is given by

$$\partial_t\theta + (\mathbf{u}\cdot\nabla)\theta = \kappa\nabla^2\theta - \mathbf{G}\cdot\mathbf{u}(\mathbf{x}, t). \tag{7}$$

III. THE MULTI-SCALE TURNOVER LAGRANGIAN MAP FOR ADVECTED SCALAR WITH LINEAR MEAN PROFILE

The multi-scale turnover Lagrangian map (MTLM) model for synthetic turbulence is motivated by the fact that the non-linear advection term in the NS equation is the key factor that generates the non-Gaussian statistics in real turbulence. The effects of this term is thus isolated and modelled as an advection map. The map is then applied to an initially Gaussian field in a multi-scale fashion to model the multi-scale interactions in real turbulence.

Keeping only the non-linear advection term, the NS equation becomes the Riemann equation

$$\partial_t\mathbf{u} + (\mathbf{u}\cdot\nabla)\mathbf{u} = 0, \tag{8}$$

which describes the evolution of non-interacting fluid particles. Eq. 8 is an approximation for high Re flows for rarefied gas[1]. The solution of the equation is

$$\mathbf{u}(\mathbf{X}(t), t) = \mathbf{u}(\mathbf{y}), \tag{9}$$

where $\mathbf{X}(t)$ is the position of a fluid particle initially at point $\mathbf{y}$, and is given by

$$\mathbf{X}(t) = \mathbf{y} + t\mathbf{u}(\mathbf{y}). \tag{10}$$

$\mathbf{u}(\mathbf{y})$ is the initial velocity field.

The solution can be concisely written in terms of an integral operator. We will call it the advection operator and denote it by $\mathcal{A}^u$:

$$\mathbf{u}_t(\mathbf{x}) = \mathcal{A}^u\mathbf{u} = \int W(\mathbf{x} - \mathbf{y} - t\mathbf{u}(\mathbf{y}))\mathbf{u}(\mathbf{y})d^3\mathbf{y}, \tag{11}$$

where we have used $\mathbf{u}_t(\mathbf{x})$ to denote the velocity at location $\mathbf{x}$ and time t. $W(\mathbf{x})$ is a weighting function, and the solution given by Eqs. 9 and 10 is obtained by choosing $W(\mathbf{x})$ as the Dirac-δ function $\delta(\mathbf{x})$. In the numerical implementation, however, a smooth $W(\mathbf{x})$ is used to approximate the Dirac-δ function. We will regard t as a parameter of the operator.

As having been emphasized before,[1,2,51] the advection operator is highly non-linear. The operator produces a non-Gaussian field as the output when it is applied to a Gaussian, structureless field.

For the scalar field, if we focus on the fluctuations over a length scale which is much larger than the Kolmogorov length scale (such as in high Re flows), the effects of molecular diffusion are negligible. The advection-diffusion equation thus becomes:

$$\partial_t\theta + (\mathbf{u}\cdot\nabla)\theta = -\mathbf{G}\cdot\mathbf{u}(\mathbf{x}, t). \tag{12}$$

The equation can be formally integrated by using Lagrangian coordinates, which gives

$$\theta(\mathbf{X}(t), t) = \theta(\mathbf{x}, 0) - \mathbf{G}\cdot\int_0^t \mathbf{u}(\mathbf{X}(t'), t')dt'. \tag{13}$$

With the approximation to the velocity field given by Eq. 9, the solution for θ becomes

$$\theta(\mathbf{X}(t), t) = \theta(\mathbf{y}) - t\mathbf{G}\cdot\mathbf{u}(\mathbf{y}), \tag{14}$$

In other words, $\mathbf{u}$ has been frozen at its value at $t = 0$. The solution can be represented by an integral operator $\mathcal{A}^s$ as follows:

$$\theta_t(\mathbf{x}) = \mathcal{A}^s\theta = \int W(\mathbf{x} - \mathbf{y} - t\mathbf{u}(\mathbf{y})) \\ (\theta(\mathbf{y}) - t\mathbf{G}\cdot\mathbf{u}(\mathbf{y}))d^3\mathbf{y}, \tag{15}$$

where we have used $\theta_t(\mathbf{x})$ to represent the scalar fluctuation field at $\mathbf{x}$ and time t. The operator $\mathcal{A}^s$ is the advection operator for the scalar field. Its expression is a new contribution of this article.

In the MTLM method, the above advection operators are applied to Gaussian random fields in a nested multi-scale fashion to produce the non-Gaussian synthetic turbulence fields. We now briefly explain the procedure and the related notations. For more information, see [14] and [3].

To begin with, we note that the MTLM procedure includes a rescaling operation that maintains the energy and scalar spectra of the fields. These spectra have to be given as part of the input, which will be denoted by $E_p^u(k)$ and $E_p^s(k)$, for energy and scalar variance spectra,

respectively. We then define a hierarchy of M decreasing length scales $\ell_n = 2^{-n}\ell_0$ $(n = 1, 2, ..., M)$, where ℓ_0 is a reference length at the order of the turbulent integral length scale of the velocity field, which is assumed to be the same as that of the scalar field. The number M is selected in such a way that $\ell_M \sim \eta$ where η is the Kolmogorov length scale. For $Sc \sim 1$, ℓ_M is sufficient to describe the dissipative scales for both the kinetic energy and the scalar variance.

For each length scale ℓ_n, we use operator $\mathcal{G}_n$

$$\mathcal{G}_n\mathbf{u}(\mathbf{x}) = \int G(\mathbf{x}-\mathbf{y})\mathbf{u}(\mathbf{y})d^3\mathbf{y}, \tag{16}$$

to denote the cut-off filter with length scale ℓ_n. We use $\mathcal{G}_n$ to extract the low wavenumber parts of the velocity and the scalar fields, $\mathcal{G}_n\mathbf{u}$ and $\mathcal{G}_n\theta$. The advection operators $\mathcal{A}^u$ and $\mathcal{A}^s$ are applied to $\mathcal{G}_n\mathbf{u}$ and $\mathcal{G}_n\theta$, whereas the high wavenumber parts are saved aside. As we have seen above, the operators contain time t as a parameter. This parameter is chosen based on the physics at the given length scale, as follows. At scale ℓ_n, the local eddy turnover time is

$$\tau_n = \ell_n^{2/3}/\langle\epsilon\rangle^{1/3}. \tag{17}$$

On the other hand, the advection time scale is

$$t_n = \ell_n/u_n' \tag{18}$$

with

$$u_n' = \left(\frac{2}{3}\int_0^{k_{c,n}} E_p^u(k)dk\right)^{1/2}, \tag{19}$$

where $k_{c,n} \equiv \pi/\ell_n$ is the cut-off wavenumber corresponding to ℓ_n. In other words, u_n' is the root-mean-square (RMS) velocity of the filtered velocity field. t_n is chosen as the time parameter for the advection maps. As is argued in [1] and [2], t_n is the time scale needed for a fluid particle to travel over the the local length scale ℓ_n , and it is only over this time period that the interactions of the particles can be reasonably neglected, as implied in the advection maps.

On the other hand, energy cascade occurs over the eddy turnover time scale τ_n. Therefore, in order to capture the effects of energy cascade, it is necessary to iterate the advection maps m_n times, where $m_n = \tau_n/t_n$, to ensure eddies are sufficiently broken down. As a consequence, the effects of interaction between the fluid particles can no longer be completely ignored. The MTLM model thus imposes incompressibility between successive applications of the advection operators, by projecting the Fourier modes of the velocity fields onto the divergence-free subspace. This projection captures the first and most important effect of the interaction between fluid particles.

We introduce the projection operator

$$\mathcal{P}\hat{\mathbf{u}}(\mathbf{k}) = [I - \hat{\mathbf{k}}\otimes\hat{\mathbf{k}}]\hat{\mathbf{u}}(\mathbf{k}), \tag{20}$$

where $\hat{\mathbf{u}}(\mathbf{k})$ is a Fourier mode of $\mathbf{u}(\mathbf{x})$, $\hat{\mathbf{k}} = \mathbf{k}/|\mathbf{k}|$ and I is the identity matrix. Then, the operator applied to the filtered velocity field at scale ℓ_n is $(\mathcal{P}\mathcal{A}_n^u)^{m_n}$, and that to the filtered scalar field is $(\mathcal{A}_n^s)^{m_n}$, where we have used subscript n to emphasize the fact that the operators are defined using time scale t_n.

Finally, to maintain the prescribed spectra, the resulted velocity and scalar fields are rescaled. We introduce the rescaling operators $\mathcal{R}_n^u$ for the velocity field and $\mathcal{R}_n^s$ for the scalar field, which are defined by

$$\mathcal{R}_n^u\hat{\mathbf{u}}(\mathbf{k}) = \left(\frac{E_p^u(k)}{E^u(k)}\right)^{1/2}\hat{\mathbf{u}}(\mathbf{k}), \tag{21}$$

and

$$\mathcal{R}_n^s\hat{\theta}(\mathbf{k}) = \left(\frac{E_p^s(k)}{E^s(k)}\right)^{1/2}\hat{\theta}(\mathbf{k}), \tag{22}$$

$E^u(k)$ and $E^s(k)$ are the energy and scalar spectra of the synthetic fields at $k = |\mathbf{k}|$, respectively. E_p^u and E_p^s are the prescribed spectra, as we have mentioned above.

Note that the above operators have been applied to the low-pass filtered fields $\mathcal{G}_n\mathbf{u}$ and $\mathcal{G}_n\theta$. The resulted velocity and scalar fields are then merged with the high wavenumber components to form the full fields, which are then filtered with $\mathcal{G}_{n+1}$ at the next length scale ℓ_{n+1} and subject to similar operations again. The procedure starts from $n = 1$ and is iterated until $n = M$. After M iterations, the final velocity field is given by

$$\mathbf{u}_e = \mathcal{M}^u\mathbf{u}, \tag{23}$$

where

$$\mathcal{M}^u = \prod_{n=1}^{M}[\mathcal{R}_n^u(\mathcal{P}\mathcal{A}_n^u)^{m_n}\mathcal{G}_n + \mathcal{G}_n^c]\mathcal{P}. \tag{24}$$

and $\mathcal{G}_n^c = 1 - \mathcal{G}_n$. The final scalar field is given by

$$\theta_e = \mathcal{M}^s\theta, \tag{25}$$

with

$$\mathcal{M}^s = \prod_{n=1}^{M}[\mathcal{R}_n^s(\mathcal{A}_n^s)^{m_n}\mathcal{G}_n + \mathcal{G}_n^c]. \tag{26}$$

$\mathcal{M}^u$ and $\mathcal{M}^s$ are the MTLM maps for the velocity and scalar fields, respectively.

IV. ANALYSIS OF SUBGRID-SCALE PROCESSES

In LES, the relevant field variables are decomposed into large- and small-scale components. This decomposition is achieved by applying spatial filtering to the field variables. Then the large scales of the flow are explicitly computed from the filtered NS equation, while the effect of the unresolved, or subgrid scales (SGS) is

modelled[4,35,52] . Applying the filtering procedure to the NS equation leads to the filtered NS equation

$$\partial_t \widetilde{u}_i + \widetilde{u}_j \partial_j \widetilde{u}_i = -\partial_i \widetilde{p} + \nu \nabla^2 \widetilde{u}_i - \partial_j \tau_{ij} + \widetilde{f}_i, \qquad (27)$$

with

$$\nabla \cdot \widetilde{\mathbf{u}} = 0. \qquad (28)$$

In the above equation, tilde denotes low-pass filtering, and $\widetilde{u}_i$ is the ith component of the filtered velocity vector, defined as

$$\widetilde{u}_i(\mathbf{x}) = \int G_\Delta(\mathbf{x}-\mathbf{y}) u_i(\mathbf{y}) d\mathbf{y}, \qquad (29)$$

with G_Δ being the filter with length scale Δ.

The effect of the subgrid scales on the resolved scales is contained in the SGS stress tensor $\tau_{ij} \equiv \widetilde{u_i u_j} - \widetilde{u}_i \widetilde{u}_j$. τ_{ij} represents the effects of the small scales, and has to be modelled. Many models have been proposed, which have been reviewed in, e.g., [35], [52], and [4]. Usually τ_{ij} is calculated explicitly as a function of certain resolved variables, such as the resolved vorticity vector $\widetilde{\omega}_i = \varepsilon_{ijk}\partial_j \widetilde{u}_k$, the resolved strain-rate tensor $\widetilde{S}_{ij} = (\partial_i \widetilde{u}_j + \partial_j \widetilde{u}_i)/2$, or the test-filtered resolved velocity field as in the so-called dynamical models. Some of the parameters may have to be found from additional transport equations. This methodology includes the eddy-viscosity-type models, similarity models, among others, with or without using the dynamic procedure. In another approach, the SGS velocity field is reconstructed by explicit estimation or approximate de-convolution (see, e.g., [54] and more recently [55]). From this reconstructed velocity field, one may calculate the approximate τ_{ij}, although its expression is not derived explicitly. The MTLM method potentially provides a new method to reconstruct the SGS velocity and scalar fields. In either case, it is important to examine the relations between the resolved quantities and the SGS stress, in order to either develop or validate the SGS models.

The SGS energy dissipation is defined as

$$\Pi \equiv -\tau_{ij} \widetilde{S}_{ij}. \qquad (30)$$

The SGS energy dissipation describes the rate of kinetic energy being transferred from the resolved to the SGS motions, and is the most important parameter that characterizes the effects of τ_{ij}[4,27,35,52]. The behavior of Π is correlated with the relative alignment between the eigenframes of SGS stress tensor τ_{ij} and filtered strain-rate tensor $\widetilde{S}_{ij}$. To see this more clearly, we denote the eigenvalues of $-\tau_{ij}$, in decreasing order, as $\alpha_{-\tau} \geq \beta_{-\tau} \geq \gamma_{-\tau}$, and the corresponding eigenvectors $\boldsymbol{\alpha}_{-\tau}$, $\boldsymbol{\beta}_{-\tau}$, and $\boldsymbol{\gamma}_{-\tau}$. The eigenvalues of $\widetilde{S}_{ij}$ are denoted by $\alpha_s \geq \beta_s \geq \gamma_s$, which are referred to as the extensive, intermediate and contracting eigenvalues, respectively. The corresponding eigenvectors are denoted by $\boldsymbol{\alpha}_s$, $\boldsymbol{\beta}_s$ and $\boldsymbol{\gamma}_s$, With these definitions, the SGS kinetic energy dissipation can be written as

$$\begin{aligned}\Pi =& \alpha_{-\tau}\alpha_s(\boldsymbol{\alpha}_{-\tau},\boldsymbol{\alpha}_s)^2 + \alpha_{-\tau}\beta_s(\boldsymbol{\alpha}_{-\tau},\boldsymbol{\alpha}_s)^2 \\ &+ \alpha_{-\tau}\gamma_s(\boldsymbol{\alpha}_{-\tau},\boldsymbol{\gamma}_s)^2 + \beta_{-\tau}\alpha_s(\boldsymbol{\beta}_{-\tau},\boldsymbol{\alpha}_s)^2 \\ &+ \beta_{-\tau}\beta_s(\boldsymbol{\beta}_{-\tau},\boldsymbol{\beta}_s)^2 + \beta_{-\tau}\gamma_s(\boldsymbol{\beta}_{-\tau},\boldsymbol{\gamma}_s)^2 \\ &+ \gamma_{-\tau}\alpha_s(\boldsymbol{\gamma}_{-\tau},\boldsymbol{\alpha}_s)^2 + \gamma_{-\tau}\beta_s(\boldsymbol{\beta}_{-\tau},\boldsymbol{\alpha}_s)^2 \\ &+ \gamma_{-\tau}\gamma_s(\boldsymbol{\beta}_{-\tau},\boldsymbol{\gamma}_s)^2, \end{aligned} \qquad (31)$$

where $(\boldsymbol{\alpha}_{-\tau},\boldsymbol{\alpha}_s)$ is the cosine of the angle between the vectors $\boldsymbol{\alpha}_{-\tau}$ and $\boldsymbol{\alpha}_s$, and similarly for others. The expression shows that the relative alignment between the eigenvectors is an important factor controlling the magnitude of Π.

For the passive scalar, we may also write down the filtered scalar transport equation

$$\partial_t \widetilde{\theta} + \widetilde{u}_i \partial_i \widetilde{\theta} = \kappa \nabla^2 \widetilde{\theta} - \partial_i \tau_i^\theta - \mathbf{G} \cdot \widetilde{\mathbf{u}}, \qquad (32)$$

where $\widetilde{\theta}$ is the filtered fluctuation of passive scalar θ defined in a way similar to $\widetilde{u}_i$. The SGS scalar flux, τ_i^θ, is defined as

$$\tau_i^\theta = \widetilde{u_i \theta} - \widetilde{u}_i \widetilde{\theta} \qquad (33)$$

Π^θ will be used to denote the SGS scalar variance dissipation that characterizes the effects of τ_i^θ. The definition of Π^θ is

$$\Pi^\theta = -\tau_i^\theta \partial_i \widetilde{\theta}. \qquad (34)$$

Similar to the SGS energy dissipation Π, Π^θ plays a central role in the SGS modelling of the SGS flux vector τ_i^θ. Its definition also shows the importance of the relative orientation between τ_i^θ and the gradient of the filtered scalar fluctuation.

In many applications, the SGS stresses τ_{ij} and the SGS fluxes τ_i^θ are the only quantities needed to be modelled. However, in some other applications, notably the LES of turbulent reactive flows[56,57], it is also necessary to model the SGS scalar variance Z_v defined as

$$Z_v \equiv \widetilde{\theta\,\theta} - \widetilde{\theta}\,\widetilde{\theta}, \qquad (35)$$

and the filtered (molecular) scalar dissipation

$$\widetilde{\epsilon}_\theta \equiv 2\kappa[\widetilde{\partial_i\theta \partial_i\theta} - \partial_i\widetilde{\theta}\partial_i\widetilde{\theta}\,]. \qquad (36)$$

These two quantities are important because they are the key parameters needed to model the chemical reaction rates of the species in a turbulent reactive flow, and the latter are crucial for the LES of such flows (for recent discussions, see, e.g., [58], [59], [60] and [61]). We will examine the statistics of Z_v in what follows. On the other hand, the statistics of $\widetilde{\epsilon}_\theta$ can be inferred from those of $\partial_i\theta$, thus will not be discussed in details.

The quantities listed above (τ_{ij}, τ_i^θ, Π, Π_θ, Z_v and related quantities) provide a comprehensive description

of the SGS processes and their interactions with the resolved ones. Once an MTLM field has been constructed, these quantities can all be calculated. We will calculate the statistics of these quantities and examine the results against DNS data. In doing so, we show that the synthetic MTLM fields capture the inter-scale interactions with good accuracy, hence potentially can be useful in SGS modelling.

V. RESULTS AND ANALYSIS

A. Parameters for the DNS and MTLM data sets

We will compare the statistics calculated from the MTLM fields with those calculated from DNS. To obtain the DNS dataset, the incompressible Navier-Stokes equation (Eq. 2) along with the advection-diffusion equations (Eq. 7) are solved by a pseudo-spectral method. The computation box is a $[0, 2\pi]^3$ cubic box with periodic boundary conditions for the velocity and for the fluctuating part of the scalar θ in three directions. The spatial resolution is 256^3. Full dealiasing is achieved through truncation according to the 2/3 rule. Energy is injected into the velocity field at a constant rate $\langle\epsilon\rangle = 0.1$ by the forcing term, which is non-zero only for Fourier modes with wavenumber $|k| \leq 2$. Statistical stationary of scalar fluctuations is achieved by the mean gradient through the source term $-\mathbf{G}\cdot\mathbf{u}$ where $\mathbf{G} = -\mathbf{e}_y$ has been chosen. In other words, the mean scalar gradient is in the negative y-direction.

Our study has been limited to the inertial-convective regime ($Sc = 1$). The viscosity is $\nu = 0.003$, which is the same as the diffusivity κ. Therefore, we have $k_{\max}\eta \approx 2.9$ where η is the Kolmogorov length scale. The simulation is thus very well resolved. Computation shows that $u_{\rm rms} = 0.7$ in the steady state, hence the Taylor Reynolds number $Re_\lambda \approx 109$.

We use the MTLM method to generate samples of the synthetic field on a periodic cubic domain $[0, 2\pi]^3$ which, in most cases, is discretized with 256^3 grid points. The 3D energy and scalar variance spectra, $E_p^u(k)$ and $E_p^s(k)$, are taken from DNS data, and are used as the input parameters. The spectra are shown in Fig. 1. Note that, due to the limit of resolution, no clearly visible inertial range is observed. Fifty synthetic fields are generated and in most cases the statistics presented are averaged over these 50 fields; some are calculated with a subset of the samples. The number of iteration levels M is chosen as 6. For more discussion of how to choose M see [14].

In what follows, we will use the Gaussian filter[4]. Unless stated otherwise, the filter scale Δ is always chosen as $\Delta = 8\delta_x$, which gives approximately $\Delta \approx 9\eta$. We have checked that the results for $\Delta = 16\delta_x \approx 18\eta$ are qualitatively the same, although occasionally we also plot the results for $\Delta = 16\delta_x$ as a comparison. The two filter scales are indicated in Fig. 1 by the vertical lines.

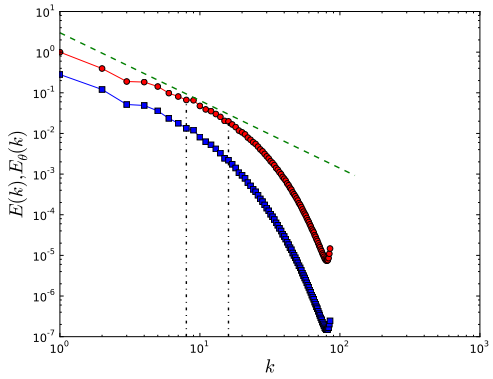

FIG. 1. Spectra for the DNS fields. Blue squares: the energy spectra $E^p(k)$. Red circles: the scalar variance spectra $E_\theta^p(k)$. Green dashed line: the Kolmogorov $-5/3$ spectrum. The two vertical dash-dotted lines indicate filter scales $\Delta = 8\delta_x$ and $\Delta = 16\delta_x$.

B. Anisotropic scalar statistics due to the mean scalar gradient

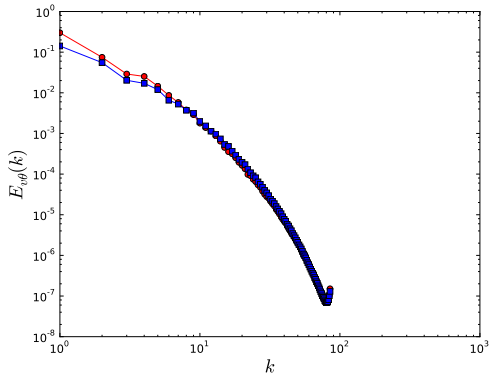

FIG. 2. The co-spectra between θ and v-velocity component. Blue squares: MTLM fields. Red circles: DNS fields.

We first present some basic scalar statistics with emphasis on the anisotropic statistics due to the mean gradient. The co-spectra between the scalar θ and the v-velocity component are presented in Fig. 2. The spectrum from MTLM fields under-predicts the DNS result slightly at the low wavenumber end. The agreement nevertheless is very good. We note that the co-spectrum for the synthetic field is not part of the input to the MTLM procedure; it is generated by the non-linear mapping embedded in the procedure, although undoubtedly, it depends crucially on the input energy and scalar spectra.

The PDF distributions of scalar gradients $\partial_l\theta$ in the synthetic MTLM fields are shown in Figs. 3 and 4. Due to statistical symmetry, the PDFs for $\partial\theta/\partial x$ and $\partial\theta/\partial z$ are expected to be the same. Fig. 3 shows indeed that the two PDFs are close to each other. There are some

discrepancies at the ends of the tails, which may be attributed to statistical fluctuations. For all PDFs in these two figures, strong deviation from a Gaussian distribution is observed, displaying the characteristic flaring tails seen in scalar turbulence[28–31]. The PDF for $\partial\theta/\partial y$ (Fig. 4) has a strong negative skewness, which means that it is skewed in the direction of the mean scalar gradient (the negative y-direction). Overall, the MTLM fields underestimate the PDFs for large fluctuations to some extent. However, all results are close to those obtained from DNS fields, as is shown by these figures (see also [15]).

The skewness is an indication of small scale anisotropy due to the negative mean gradient. It has been correlated to the observation that the cliffs in the scalar distribution sit on the edges of the vortices in the velocity field[15,22]. We may also understand it qualitatively from the equation for $g_y \equiv \partial\theta/\partial y$, which is

$$\partial_t g_y + \mathbf{u}\cdot\nabla g_y = -(\partial_y \mathbf{u})\cdot\nabla\theta + \kappa\nabla^2 g_y + \partial_y v \qquad (37)$$

where v is the y component of the velocity field, and we have used the fact that the mean scalar gradient $\mathbf{G} = -\mathbf{e}_y$. The last term on the right hand side represents the direct contribution from the mean scalar gradient. Note that $\partial_y v$ is the longitudinal gradient of v. It is well-known that, in real turbulence, the longitudinal gradient of the velocity has a negative skewness. The same has been observed in MTLM velocity fields too[1]. As such, the last term on the right hand side of Eq. (37) is more likely to be negative, which tends to reduce g_y. This term thus provides a driving mechanism for the negative skewness in the PDF of g_y that is absent from other components of the gradient. Fig. 4 shows that the same mechanism is captured by the MTLM procedure, although results for the MTLM fields appear to somewhat underestimate the probabilities for large fluctuations.

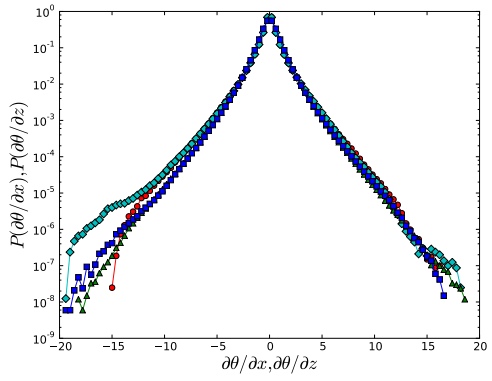

FIG. 3. PDFs for scalar gradients. Blue squares: $\partial\theta/\partial x$ from MTLM fields. Red circles: $\partial\theta/\partial x$ from DNS fields. Green triangles: $\partial\theta/\partial z$ from MTLM fields. Cyan diamonds: $\partial\theta/\partial z$ from DNS.

The source term in the equation of θ is $-\mathbf{G}\cdot\mathbf{u} = v$, according to Eq. 7. By writing down the equation for $\langle\theta^2\rangle$ (not shown), we can see that, to provide a positive source

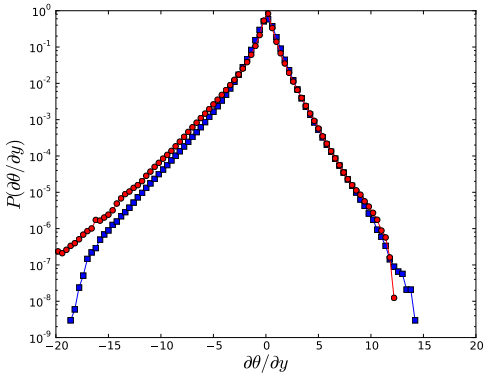

FIG. 4. PDFs for $\partial\theta/\partial y$. Green squares: MTLM fields. Red circles: DNS fields.

for the scalar fluctuations, a positive correlation must exist between v and scalar θ. The PDFs of the normalized product $r_\theta \equiv v\theta$, from both DNS and MTLM fields, are presented in Fig. 5. As expected, both PDFs displays a positive skewness. The positive skewness is consistent with the co-spectrum shown in Fig. 2, both indicating a positive correlation between v and θ. A physical explanation for the positive correlation is given in [53] using a Lagrangian closure. Intuitively, positive fluctuation of θ at a point is generated when a parcel of fluid carrying a larger value of the scalar moves to the point. Given that the mean gradient of the scalar is in the negative y direction, this parcel is more likely to come from the negative y direction. Thus, on average, this parcel will have a positive v on its path to this point. Given the positive spatial correlation of v, it is also more likely that v is positive at the given point. Thus we observe positive v together with positive θ, hence positive correlation between the two. Fig. 5 shows that the mechanism is captured very well by the MTLM fields.

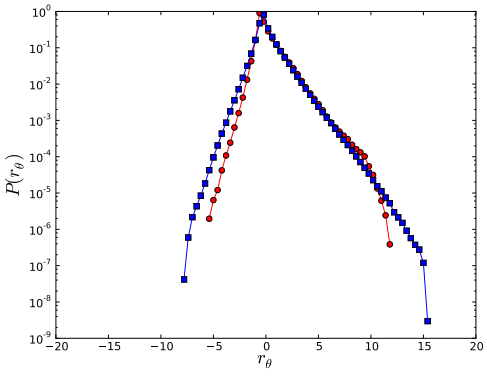

FIG. 5. The PDFs of the normalized fluctuating flux r_θ. Blue squares: MTLM fields. Red circles: DNS fields.

C. SGS energy dissipation, scalar variance dissipation and scalar variance

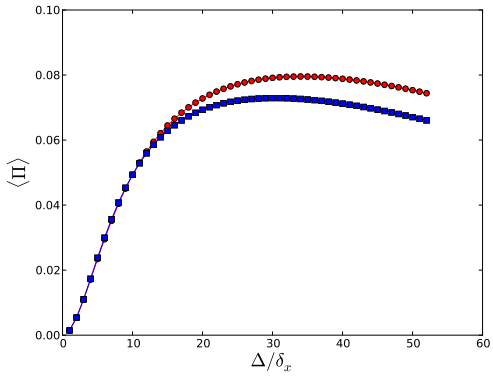

FIG. 6. Mean SGS energy dissipation rate $\langle\Pi\rangle$ as a function of filter scale Δ (δ_x is the grid size of the simulation): Blue squares: MTLM fields. Red circles: DNS fields.

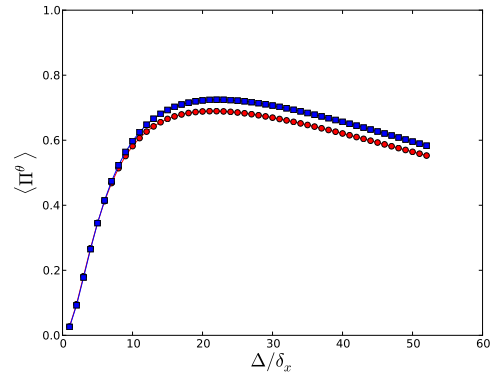

FIG. 7. Mean SGS scalar variance dissipation rate $\langle\Pi^\theta\rangle$ as a function of filter scale Δ (δ_x is the grid size): Blue squares: MTLM fields. Red circles: DNS fields.

The mean SGS energy dissipation rate $\langle\Pi\rangle$ as a function of the filter scale Δ is shown in Fig. 6, while the mean SGS scalar variance dissipation rate $\langle\Pi^\theta\rangle$ is shown in Fig. 7. For the scalar dissipation, the agreement between MTLM results and DNS results is rather good with some small over-prediction (at about 3%). For the velocity fields, the MTLM results underestimate the DNS values by a small amount, which measures at about 10% at the largest filter scales. The fact that the prediction for SGS scalar dissipation is better may be explained by the following observation. The synthesized velocity field is missing both viscous diffusion and the nonlocal effect of the pressure. The synthesized scalar field, on the other hand, is missing only the diffusion effect. Though these effects are partially compensated for by imposing the energy and scalar spectra, the approximation to the velocity fields is still stronger.

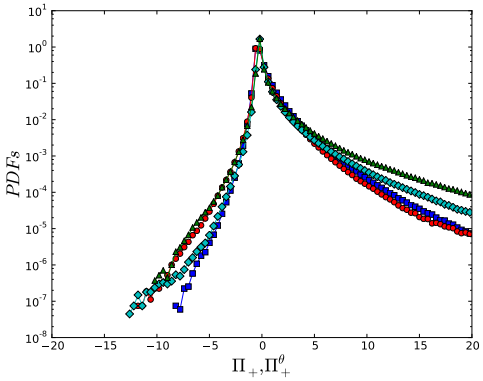

FIG. 8. The PDFs of the normalized SGS energy dissipation $\Pi_+ = (\Pi - \langle\Pi\rangle)/\sigma_\Pi$ and the normalized SGS scalar variance dissipation $\Pi^\theta_+ = (\Pi^\theta - \langle\Pi^\theta\rangle)/\sigma_{\Pi^\theta}$. Blue squares: PDF of Π_+ for MTLM fields. Red circles: PDF of Π_+ for DNS fields. Cyan diamonds: PDF of Π^θ_+ for MTLM fields. Green triangles: PDF of Π^θ_+ for DNS fields.

The PDFs for both the SGS energy and SGS scalar variance dissipations are shown in Fig. 8. We use $\Pi_+ = (\Pi - \langle\Pi\rangle)/\sigma_\Pi$ to represent the normalized SGS energy dissipation, where $\langle\Pi\rangle$ is the mean and σ_Π is the r.m.s. of Π. A similar notation Π^θ_+ denotes the normalized SGS scalar dissipation. The PDFs from MTLM fields are shown with blue squares and cyan diamonds, whereas DNS fields are shown with red circles and green triangles. The strong positive skewness observed in the curves indicates the dominance of forward energy and scalar variance cascade. A significant probability for negative fluctuations is also observed (flaring up left tail), which indicates a backscattering from small scales to large ones. The PDF of Π^θ_+ has a slightly wider positive tail than that of Π_+ from the same data set (either MTLM or DNS). The MTLM fields capture all these behaviours. Quantitatively, the positive tail for Π_+ agrees rather well with DNS result, though the negative tail is somewhat underestimated for both the scalar variance and energy dissipations.

To quantify the backscattering, we calculate separately the mean of the negative SGS dissipation (denoted by $\Pi^{<0}$) and the mean of positive SGS dissipation (denoted by $\Pi^{>0}$), and look into their relative magnitudes, given by ratio

$$\frac{\langle|\Pi^{<0}|\rangle}{\langle|\Pi^{<0}|\rangle + \langle|\Pi^{>0}|\rangle}. \tag{38}$$

We calculate the ratio for both velocity and scalar fields from both MTLM and DNS data. Fig. 9 shows a plot of the ratio as a function of Δ. One can observe from the figure that MTLM fields indeed generate significant backscattering, as in DNS fields. For the velocity fields, the ratio tends to 0.20 for both MTLM and DNS fields when Δ increases, although for smaller Δ MTLM results somewhat underestimate the value. For the scalar fields,

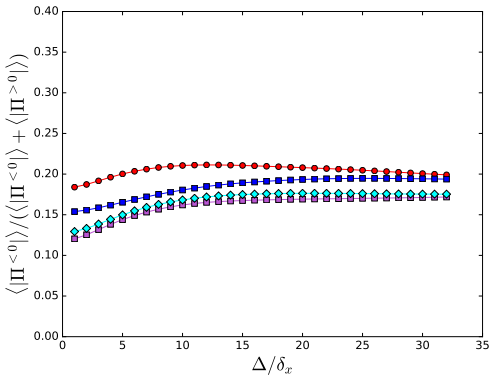

FIG. 9. The proportion of backscattering defined by $\langle|\Pi^{<0}|\rangle/\langle|\Pi^{<0}|\rangle+\langle|\Pi^{>0}|\rangle$ as a function of filter scale Δ (δ_x is the grid size). Blue squares and red circles: SGS energy dissipation for MTLM and DNS fields, respectively. Cyan diamonds and medium-orchid squares: SGS scalar variance dissipation for MTLM and DNS fields, respectively.

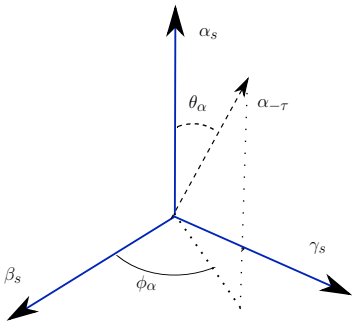

FIG. 10. Definitions of θ_α and ϕ_α for the two-dimensional joint PDF characterizing the alignment of the vector $\boldsymbol{\alpha}_{-\tau}$ with the eigenvectors of tensor $\widetilde{S}_{ij}$.

the ratio tends to around 0.18 for MTLM fields and 0.17 for DNS fields, i.e., it is overestimated slightly in the MTLM fields.

The above results regarding the SGS energy dissipation rates can be complemented by the statistics of the alignment between the eigenvectors of the tensors, as is indicated by Eq. 31. We will present the results in terms of the orientations of the eigenvectors of the SGS stress tensor $-\tau_{ij}$ in the eigenframe of the filtered strain rate tensor $\widetilde{S}_{ij}$. To describe the orientation of the eigenvector $\boldsymbol{\alpha}_{-\tau}$ in the eigenframe of $\widetilde{S}_{ij}$, we need two angles ϕ_α and θ_α[16,32,33], as can be seen in Fig. 10. Note that three dimensional joint PDFs of the three angles describing the relative orientation of the two eigenframes have also been used (see, e.g., [32]). The 3D joint PDFs have the advantage of providing a direct picture of the relative orientation of the frames. Nevertheless, quantitative details are sometimes obscured by the 2D projection of a 3D distribution. We thus choose to use 2D joint PDFs

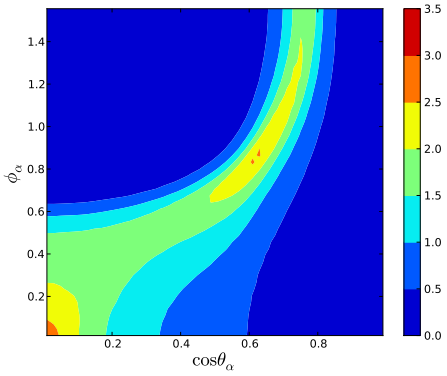

FIG. 11. Joint PDF of ($\cos\theta_\alpha$, ϕ_α) from DNS fields.

in what follows.

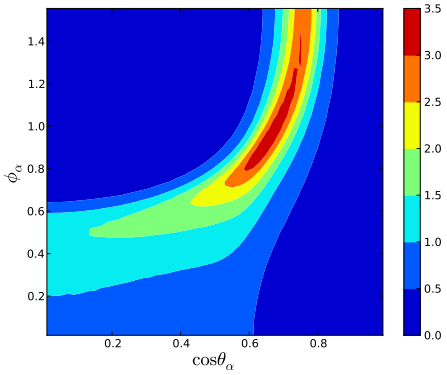

FIG. 12. Joint PDF of ($\cos\theta_\alpha$, ϕ_α) for MTLM fields.

To observe the preferential alignment configurations between $\boldsymbol{\alpha}_{-\tau}$ and the eigenframe of $\widetilde{S}_{ij}$, Fig. 11 shows the two-dimensional joint PDF of $\cos\theta_\alpha$ and ϕ_α for DNS fields. It displays a bi-modal distribution with two peaks at $(\theta_\alpha, \phi_\alpha) = (90°, 0°)$ and $(50°, 48°)$, with approximate peak value 2.5 for both. As a comparison, the MTLM result, given in Fig. 12, shows only one peak at approximately $(50°, 48°)$, which is the same as one of the peaks in the DNS result. The peak value for the MTLM result is stronger than the one for DNS, reaching about 3.5, as is illustrated by Fig 12. This discrepancy is most likely due to the fact that MTLM fields produce insufficient vortex tubes[2].

We now consider the orientation of the eigenvector $\boldsymbol{\beta}_{-\tau}$ in the eigenframe of $\widetilde{S}_{ij}$, which is characterised by angles θ_β and ϕ_β. The two angles are defined in the same way as those shown in Fig. 10. Two peaks at $(\theta_\beta, \phi_\beta) = (90°, 0°)$ and $(45°, 90°)$ are seen in Fig. 13 for the DNS fields, with peak values 1.6 and 2.0, respectively. The joint PDF for the MTLM fields shows two peaks at about the same locations (see Fig. 14). However, the peak values are approximately 2.4 and 1.6, i.e., the strengths of the two

peaks are reversed.

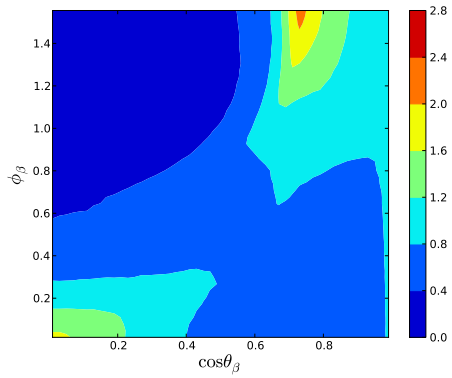

FIG. 13. Joint PDF of $(\cos\theta_\beta, \phi_\beta)$ for DNS fields.

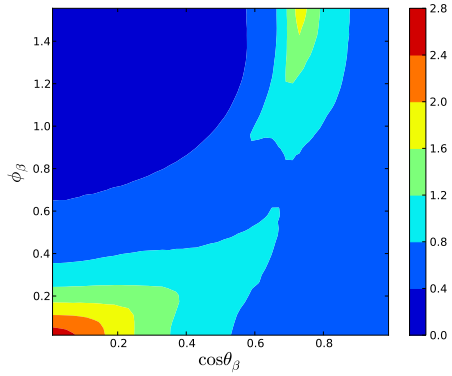

FIG. 14. Joint PDF of $(\cos\theta_\beta, \phi_\beta)$ for MTLM fields.

Finally, without showing the figure, we briefly summarize the results about the joint PDFs of the orientation of the eigenvector $\boldsymbol{\gamma}_{-\tau}$. The main observation is that, for both DNS and MTLM fields, the peaks of the joint PDFs are found at the same location $\phi_\gamma \approx 90°$ and $\theta_\gamma \approx 42°$, with peak values 9.0 and 10.5 respectively. Angles θ_γ and ϕ_γ are defined again in the same way as before.

Similar analysis can be conducted for the scalar SGS dissipation. The PDFs of the cosine of the angle between the SGS scalar flux vector τ_i^θ and the gradient of the filtered scalar $\partial_i\widetilde{\theta}$ are shown in Fig. 15, where we have used Λ^θ to denote the angle. The PDFs for both MTLM and DNS data display the same preferred alignment at $\cos\Lambda^\theta \approx 0.3$, corresponding roughly to $\Lambda^\theta = 72°$. Thus the SGS scalar flux vector does not align perfectly with the resolved scalar gradient, in contradiction with what is implied in an eddy diffusivity model. On the other hand, the peak value of the PDF from MTLM fields is somewhat higher than the DNS value.

To briefly summarize, the above results for the relative orientation of the eigenvectors calculated from the MTLM fields bear close resemblance to those from DNS

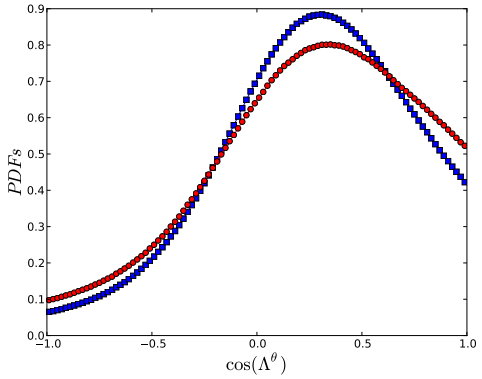

FIG. 15. PDFs of the cosine of the angle between τ_i^θ and $\partial_i\widetilde{\theta}$, Λ^θ. Blue squares: MTLM fields. Red circles: DNS fields.

fields. Some discrepancies exist in terms of the alignment results, and they are consistent with previously known features of the MTLM fields. Nevertheless, the discrepancy has only small effects on the SGS dissipation rates. These results reveal the ability of the MTLM procedure to reproduce SGS dissipations and the geometrical structures of the SGS stress and scalar flux.

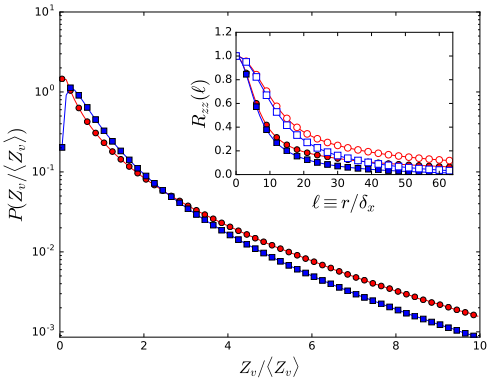

FIG. 16. PDFs of $Z_v/\langle Z_v\rangle$ for $\Delta = 8\delta_x$. Blue squares: MTLM fields. Red circles: DNS fields. The inset is the two-point correlation coefficient for Z_v. Blue squares: MTLM. Red circles: DNS. Filled and empty symbols are for $\Delta = 8\delta_x$ and $16\delta_x$, respectively.

We now present results related to the SGS scalar variance Z_v. Note that the mean of Z_v, $\langle Z_v\rangle$, is determined by the scalar spectrum. Therefore, by design, it is the same for the MTLM fields and the DNS fields. However, it is interesting to examine statistics beyond the mean. Fig. 16 compares the PDFs for Z_v calculated from the MTLM fields (blue squares) and DNS data (red circles). It shows that the MTLM fields underestimate the probability of large values. This mild discrepancy is consistent with some of the results shown previously, where MTLM fields have also been found to under-estimate large fluctuations to some degree. The MTLM fields also show

a low probability for Z_v very close to zero, whereas in DNS fields, the most probable value is $Z_v = 0$. The inset shows the correlation coefficient for Z_v, defined as

$$R_{zz}(r) = \frac{\langle [Z_v(\mathbf{x}) - \langle Z_v \rangle][Z_v(\mathbf{x}+r\mathbf{e}) - \langle Z_v \rangle] \rangle}{\langle [Z_v(\mathbf{x}) - \langle Z_v \rangle]^2 \rangle}, \quad (39)$$

plotted against the displacement r normalized by δ_x, where in the definition $\mathbf{e}$ is a given direction. Results for both $\Delta = 8\delta_x$ and $16\delta_x$ are shown. As is expected, the correlation is stronger for larger filter scales. The correlation of the MTLM fields decays somewhat quicker than that of the DNS fields, i.e., the MTLM fields somewhat underestimate the long range correlations in the scalar fields.

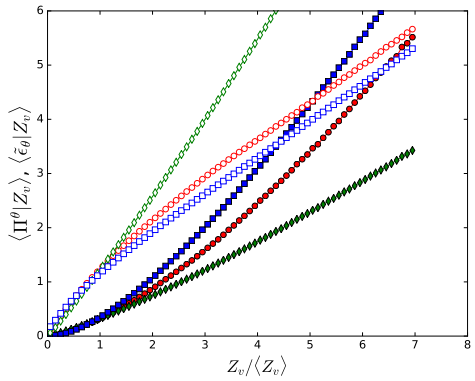

FIG. 17. Conditional averages for $\Delta = 8\delta_x$. Filled symbols: $\langle \Pi^\theta | Z_v \rangle$. Empty symbols: $\langle \widetilde{\epsilon}_\theta | Z_v \rangle$. Blue squares: MTLM fields. Red circles: DNS fields. Green diamonds: reference models (see text).

The evolution of Z_v is dominantly controlled by the SGS scalar dissipation Π^θ and the filtered (molecular) scalar dissipation $\widetilde{\epsilon}_\theta$, which provide the source and the sink terms for Z_v, respectively. To predict the PDF of Z_v correctly, the conditional averages $\langle \Pi^\theta | Z_v \rangle$ and $\langle \widetilde{\epsilon}_\theta | Z_v \rangle$ need to be correctly parametrized. Thus we have calculated the conditional averages, shown in Fig. 17. To put the results from the MTLM fields in context, the results from two other models are also presented for reference. For $\langle \Pi^\theta | Z_v \rangle$, an eddy-diffusivity-type model

$$\tau_i^\theta = c_\tau \Delta^2 |\widetilde{\mathbf{S}}| \partial_i \widetilde{\theta} \quad (40)$$

is used, where $|\widetilde{\mathbf{S}}| \equiv (2\widetilde{S}_{ij}\widetilde{S}_{ij})^{1/2}$ is the modulus of $\widetilde{S}_{ij}$. The result from this model is shown with filled green diamonds. In SGS modelling, the coefficient c_τ is usually calculated from the dynamic procedure. Here, we choose c_τ empirically, so that the model result matches the DNS result (shown with filled red circles) at $Z_v/\langle Z_v \rangle = 1$. This simple choice is sufficient to show that the model does not provide consistent prediction for $\langle \Pi^\theta | Z_v \rangle$, because it underestimates the latter, and the discrepancy increases with Z_v. Meanwhile, the result from MTLM fields overestimates $\langle \Pi^\theta | Z_v \rangle$ by a rather significant amount. Nevertheless, the discrepancy is smaller than that of the reference model, especially at large Z_v.

For $\langle \widetilde{\epsilon}_\theta | Z_v \rangle$, we choose

$$\widetilde{\epsilon}_\theta = c_\epsilon \frac{Z_v}{\tau_\epsilon} \quad (41)$$

as the reference model, where the time scale τ_ϵ is taken as $|\widetilde{\mathbf{S}}|^{-1}$ (see, e.g., [57] and [59]). c_ϵ is chosen in the same way as c_τ above. In this case, the MTLM result (empty blue squares) follows quite closely with the DNS result (empty red circles), whereas the result from the reference model (empty green diamonds) is off by large amount.

D. Geometrical statistics of SGS stresses and fluxes

In this subsection, we report on how the geometrical statistics related to the SGS stresses and fluxes are captured by the MTLM fields. Overall, the MTLM fields reproduce many alignment statistics accurately, including $\tau_i^\theta - \widetilde{\omega}_i$, $\tau_i^\theta - \widetilde{S}_{ij}$, $\tau_i^\theta - \tau_{ij}$, $\widetilde{\omega}_i - \tau_{ij}$, and $\widetilde{\omega}_i - \widetilde{S}_{ij}$ alignment. In what follows, we present only the first three results as an illustration. The PDFs of the cosine of the angle Λ^θ between SGS scalar flux vector τ_i^θ and the filtered vorticity vector $\widetilde{\omega}_i$ is given in Fig. 18. The PDFs have a sharp peak at zero, which means that the SGS scalar flux tends to be perpendicular to the filtered vorticity. The MTLM result shows good quantitative agreement with the DNS result.

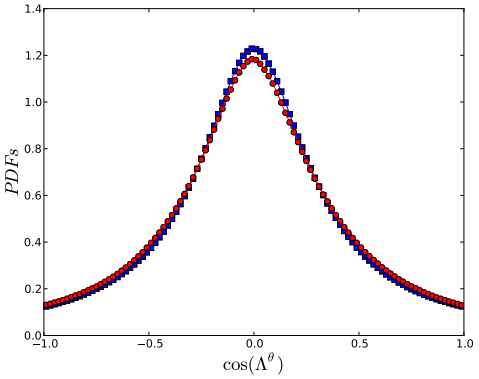

FIG. 18. PDFs of the cosine of the angle between τ_i^θ and $\widetilde{\omega}_i$, Λ^θ. Blue squares: MTLM fields. Red circles: DNS fields.

Fig. 19 shows the PDFs of the cosines of the angles between the SGS scalar flux τ_i^θ and the three eigenvectors $\boldsymbol{\alpha}_s$, $\boldsymbol{\beta}_s$ and $\boldsymbol{\gamma}_s$ of the filtered strain-rate tensor $\widetilde{S}_{ij}$. The angles are denoted by Λ_α, Λ_β and Λ_γ. Both DNS and MTLM results are plotted. The comparison shows that the results of MTLM fields are close to the DNS results. It is observed that τ_i^θ tends to make a 53° angle with $\boldsymbol{\alpha}_s$, and a 37° angle with $\boldsymbol{\gamma}_s$, whereas τ_i^θ tends to be perpendicular to $\boldsymbol{\beta}_s$.

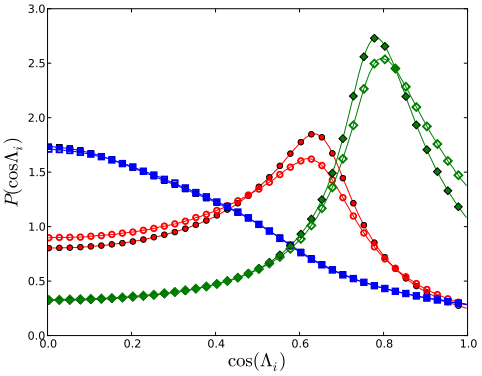

FIG. 19. PDFs of the cosine of the angles between τ_i^θ and the eigenvectors of $\widetilde{S}_{ij}$ from DNS fields (empty symbols) and MTLM fields (filled symbols). Red circles: $P(\cos\Lambda_\alpha)$. Blue squares: $P(\cos\Lambda_\beta)$. Green squares: $P(\cos\Lambda_\gamma)$.

The preferential alignment between the SGS scalar flux vector τ_i^θ and the eigenvectors of the SGS stress tensor τ_{ij} is presented in Fig. 20. Note that, for simplicity, we have used same notations for the angles as in previous figure. Here, the PDFs from MTLM fields nearly overlap with those from DNS fields, except that the peaks are slightly underestimated by MTLM (the peaks have been truncated hence are not shown in the figures). τ_i^θ tends to align with $\boldsymbol{\gamma}_{-\tau}$ with very high probability. On the other hand, τ_i^θ tends to be perpendicular to both $\boldsymbol{\alpha}_{-\tau}$ and $\boldsymbol{\beta}_{-\tau}$, but with a higher probability for the former. The high peak probabilities suggest a near deterministic alignment. This trend has been observed previously, and has motivated a strategy to model τ_i^θ in terms of τ_{ij}[34].

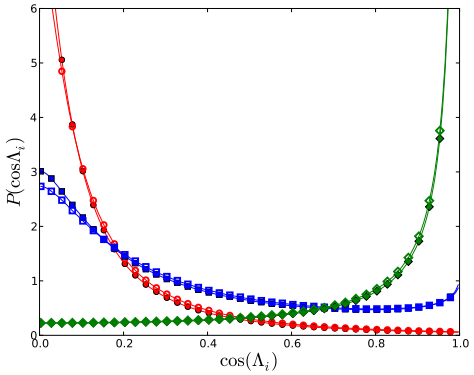

FIG. 20. PDFs of the cosine of the angles between τ_i^θ and the eigenvectors of $-\tau_{ij}$ for DNS fields (empty symbols) and MTLM fields (filled symbols). Red circles: $P(\cos\Lambda_\alpha)$. Blue squares: $P(\cos\Lambda_\beta)$. Green squares: $P(\cos\Lambda_\gamma)$.

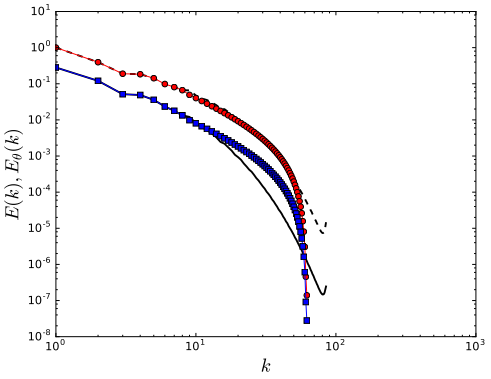

FIG. 21. The Kovasznay energy (blue squares) and scalar variance (red circles) spectra. The lines are the DNS spectra. Solid line: energy spectrum. Dashed line: scalar variance spectrum.

E. Effects of input energy and scalar spectra

In previous subsections, we have used the energy and scalar spectra from the 256^3 DNS data set as the input for the MTLM procedure. When MTLM is applied in a more practical setting, the input spectra may have to be estimated, hence contain errors. It is thus important to understand the effects of the input spectra. To achieve this, we now examine the MTLM fields with input spectra modified in two different ways. In one case, we consider MTLM fields generated from only parts of the DNS spectra shown in Fig. 1. Specifically, we generate MTLM fields with 64^3 grid points using the spectra in Fig. 1 in the range $k \in [1, 32]$ as the input. Also, we generate MTLM fields with 128^3 grid points using the spectra in the range $k \in [1, 64]$ as the input. These fields are missing most of the dissipation range due to the truncations. In another case, we use an analytical spectrum with a model for the dissipation range as the input. For the velocity field, we use the Kovasznay spectrum[62], whose expression can be written as[63]:

$$E(k) = C_k \langle\epsilon\rangle^{2/3} k^{-5/3} \left[\left(1 - \frac{C_k}{2}(k\eta)^{4/3}\right)^2\right]. \qquad (42)$$

In other words, the spectrum is the Kolmogorov spectrum corrected for viscous dissipation by the factor in the square brackets. For scalar, we assume the spectrum is given by Eq. 5 multiplied by the same correction factor. To ensure that this case can be compared with previous results, an empirical modification is applied. Namely, we use Eq. 42 (and its scalar equivalence) for $k \geq 8$ only; the spectrum for $k \leq 8$ is still taken from DNS data. The dissipation rates in the Kovasznay spectra are chosen in such a way that the two segments join together smoothly. The spectra constructed this way are plotted in Fig. 21.

We use the model spectra to generate 256^3 MTLM fields. The Kovasznay spectrum is reasonably realistic

Dataset	Description
M64	64^3 MTLM fields with truncated DNS spectra as input
M128	128^3 MTLM fields with truncated DNS spectra as input
M256	256^3 MTLM fields with full DNS spectra as input
MKov	256^3 MTLM fields with Kovasznay spectra as input
DNS	256^3 DNS fields

TABLE I. Datasets and descriptions.

but still deviates significantly from the observed turbulent energy spectrum. Therefore it is a relevant yet stringent test. To help with exposition, we summarize all the data sets used in this subsection in Table I, along with their names.

We show in Fig. 22 the co-spectra between the scalar θ and the y-velocity component. It can be seen that the agreement between the three resolutions is very good, all following closely with the DNS result. One may discern that the spectra of M64 and M128 are slightly lower than that of M256, but the effect is really very small. Since the M64 and M128 fields, with 64^3 and 128^3 grid points, are obtained with few iterations than the M256 fields, this shows that number of iterations is not essential for the development of the proper correlation between the scalar field and the advecting velocity. Such correlation must come basically from the strong coupling between the scalar and velocity mappings, rather than from the mimicked cascade process. This is corroborated by the result from MKov data. Here the co-spectrum at the high wavenumber end displays similar features as the Kovasznay energy and scalar spectra, where it bulges upward before dropping off sharply.

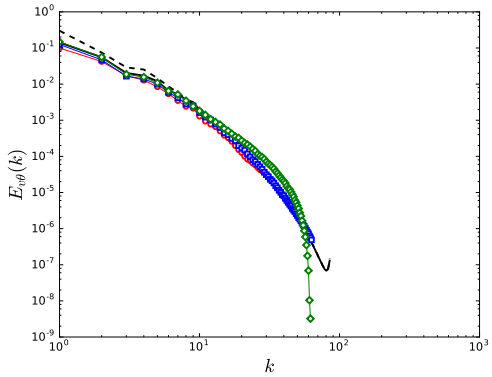

FIG. 22. The co-spectra between θ and y-velocity component. Black solid line: 256^3 MTLM fields. Black dashed line: 256^3 DNS. Red circles: 64^4 MTLM fields. Blue squares: 128^3 MTLM fields. Green diamonds: from Kovasznay spectra.

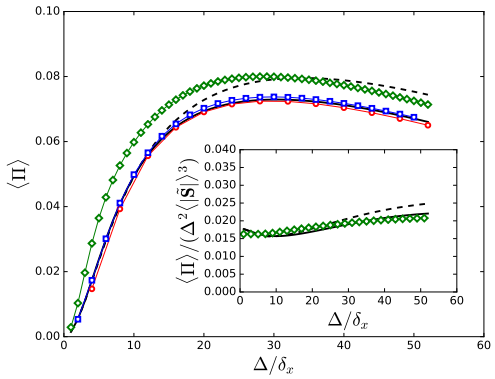

FIG. 23. The averaged SGS energy dissipation as a function of filter scale Δ. Symbols and colors are the same as in Fig. 22. The inset shows $\langle\Pi\rangle$ normalized by $\Delta^2\langle|\widetilde{\mathbf{S}}|\rangle^3$.

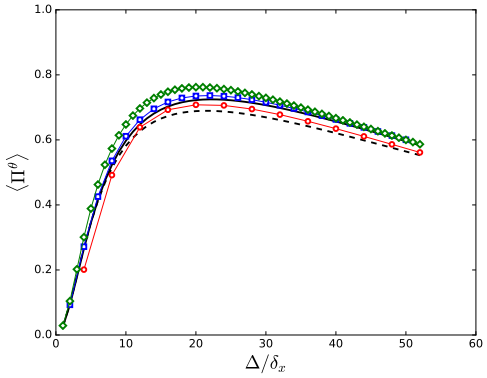

FIG. 24. Same as Fig. 23 but for the SGS scalar variance dissipation.

The mean SGS energy dissipation as a function of the filter scales is shown in Fig. 23. The truncation has little effect on $\langle\Pi\rangle$, since the results for M64, M128 and M256 all collapse on the same curve. On the other hand, the result from MKov fields deviates significantly from the one from M256, and the difference is observed over all Δ values. To understand the deviation, we plots in the inset $\langle\Pi\rangle$ from MKov, M256 and DNS, normalized by $\Delta^2\langle|\widetilde{\mathbf{S}}|\rangle^3$. Interestingly, now the results for MKov and M256 show much better agreement. Since the factor $\Delta^2\langle|\widetilde{\mathbf{S}}|\rangle^3$ is determined by the energy spectrum, the observation implies that the deviation in $\langle\Pi\rangle$ comes mainly from the difference between the Kovasznay spectrum and the DNS spectrum, and it can be parametrized by the spectrum in a simple way. Of course, how to find a good approximation for the spectrum remains a question. Though it is in no way easy, this question is a standard one with much previous research to be drawn upon. Therefore, the observation from this figure is encouraging.

Fig. 24 shows that truncation has slightly stronger effects on the scalar SGS dissipation $\langle\Pi^\theta\rangle$. In particu-

lar, the M64 fields produce slightly but visibly smaller values. The result from MKov fields is close to the M256 results, with slight over-estimation for approximately $10 \leq \Delta/\delta_x \leq 30$. This observation is not surprising, since the scalar Kovasznay spectrum is not too different from the DNS scalar spectrum (cf. Fig. 21).

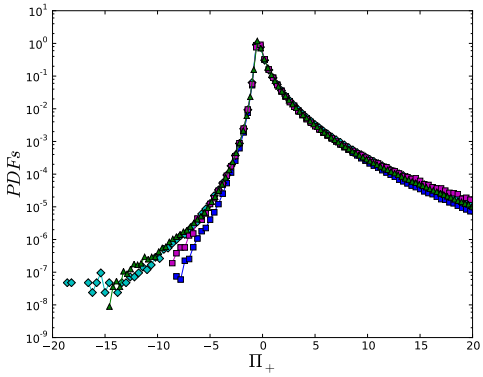

FIG. 25. The PDFs of the normalized SGS energy dissipation: $\Pi_+ = (\Pi - \langle\Pi\rangle)/\sigma_\Pi$. Blue squares: 256^3 MTLM fields. Cyan diamonds: 128^3 MTLM fields. Medium-orchid squares: 64^3 MTLM fields. Green triangles: from the Kovasznay spectra.

The PDFs of the normalized SGS energy dissipation Π_+ are given in Fig. 25. These results show that the strong positive skewness remains mostly unchanged by the change in input energy spectrum. Some differences can be discerned for the probabilities of large negative fluctuations. Apart from the result from KKov, the probabilities for large negative fluctuations seem to decrease with increasing resolutions. Note that the difference between M256 data and M64 (or M128) is that, in the latter, the small scales in the dissipation range are decimated or absent. Thus the above observation is consistent with the notion that the scales much smaller than the filter scale can be modelled by an eddy-viscosity-type model, since their overall effects are dissipative and reducing backscattering. Nevertheless, we caution against drawing definite conclusions because statistical fluctuations are relatively large at the tails of the PDFs. In any case, the effects are rather small. The PDFs for the normalized SGS scalar variance dissipation, Π^θ_+, show again little difference for the different data sets, therefore the figure has been omitted.

The conditional average $\langle\widetilde{\epsilon}_\theta|Z_v\rangle$ is shown in Fig. 26. This result is particularly interesting, because the dominant contribution to $\widetilde{\epsilon}_\theta$ comes from the dissipation range, and as such one expects that the changes in the input spectra would have stronger effects. Indeed, the result from M64 shows significant deviation from the M256 and DNS results. The result from M128 stays closer to that of M256, arguably because the truncation is less severe and part of the dissipation range is retained. The result from MKov is not much changed from that of M256 either. The inset shows the same results with $\Delta = 16\delta_x$.

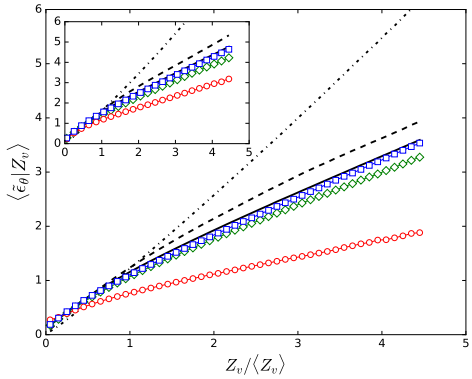

FIG. 26. Conditional average $\langle\widetilde{\epsilon}_\theta|Z_v\rangle$ with $\Delta = 8\delta_x$ (main figure) and $16\delta_x$ (inset). Red circles: 64^3 MTLM fields. Blue squares: 128^3 MTLM fields. Green diamonds: from Kovasznay spectra. Solid line: 256^3 MTLM fields with DNS spectra. Dashed line: DNS result. Dash-dotted line: reference model (Eq. 41) calculated from DNS data.

Same trends are observed, but results from MTLM fields agree better with the DNS results. The results shown in this figure suggest that a reasonably accurate model spectrum can provide a good approximation to $\langle\widetilde{\epsilon}_\theta|Z_v\rangle$.

Finally, we note that we have also looked into the geometrical statistics for these new datasets as in previous subsections. The general observation is that all data sets reproduce the preferred alignment configurations in DNS, although the probabilities for the preferred configurations become weaker when the resolution is decreased (from 256^3 to 64^3). We present only Fig. 27 to illustrate the above observation. Fig. 27 shows the PDFs of $\cos\Lambda_\alpha = (\boldsymbol{\alpha}_{-\tau}, \tau_i^\theta)$ from M256, M128 and M64 fields. All three PDFs show the same preferred alignment at $\cos\Lambda_\alpha = 0$, the two vectors being perpendicular to each other. However, the peak probability decreases with the resolution, as we mention above.

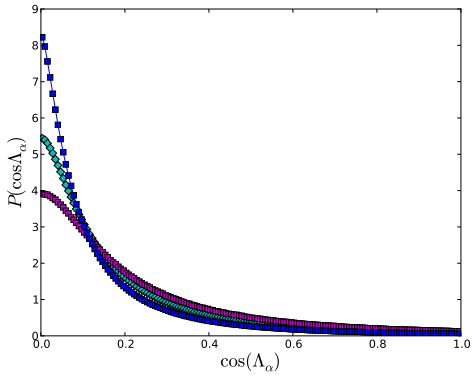

FIG. 27. PDFs of the cosine of the angles between τ_i^θ and the eigenvector of $\boldsymbol{\alpha}_{-\tau}$. Blue squares: 256^3 MTLM fields. Cyan diamonds: 128^3 MTLM fields. Medium-orchid squares: 64^3 MTLM fields.

VI. CONCLUSIONS

In this paper, the multi-scale turnover Lagrangian map is generalized to synthesize passive scalar fields driven by a uniform mean scalar gradient. The synthetic velocity and scalar fields are then investigated from the perspective of SGS modelling. We calculate the statistics related to the SGS stress, the SGS scalar flux, and the SGS scalar variance obtained by filtering the synthetic MTLM fields. We also look into how the synthetic fields are affected by the input spectra.

Comparisons with DNS data show that the resultant non-Gaussian MTLM fields display many properties commonly observed in DNS data, including the skewed and intermittent probability density distributions for the SGS dissipation rates, the preferential alignment between different objects, the scalar-velocity correlations, and the skewness of the scalar gradient in the direction of mean gradient. The results obtained from fields with different spectra as the input demonstrate the robustness of the MTLM procedure. Some statistics, such as the mean SGS energy dissipation, depend rather strongly on the energy spectrum. However, the dependence may be parametrized in a relatively simple way by the energy spectrum. The implication is that, in order to apply MTLM in a different flow, the main task is to estimate the energy and the scalar spectra. While it is by no mean easy, the task is a standard one, and many modelling strategies make implicit assumption about the spectra in some way (examples include, e.g., the scale dependent SGS model[64]). Therefore we believe it is totally feasible. More importantly, we also find that most of the statistics are unchanged by the input spectra, including the PDFs of the SGS energy and scalar dissipations. This observation is another incentive to further pursue the MTLM method.

Our investigation also shows that the linear mean scalar profile can be modelled by the MTLM procedure easily with little additional computation cost. It demonstrates that the MTLM can be generalized to include other linear effects without difficulties. This study complements previous discussions (see [1], [2], and [14] for discussions on other properties) on this technique, and provides solid basis for its applications in LES and SGS modelling. Future research will focus on technical challenges such as, among others, the modelling of inhomogeneous flows, where no complete information regarding the spectra is available. In such cases, one may have to estimate the spectra from the resolved the scales, and make use of the physics of the flows. How to implement such a scheme, and assess the performance of MTLM in these flows, are topics of our on-going research.

VII. ACKNOWLEDGMENTS

The first author acknowledges the financial support from the Iraqi government via the Ministry of High Education and Scientific Research Scholarship.

[1] C. Rosales and C. Meneveau, "A minimal multiscale Lagrangian map approach to synthesize non-Gaussian turbulent vector fields," Phys. Fluids **18**, 075104 (2006).
[2] C. Rosales and C. Meneveau, "Anomalous scaling and intermittency in three-dimensional synthetic turbulence," Phys. Rev. E **78**, 016313 (2008).
[3] Y. Li and C. Rosales, "Constrained multi-scale turnover Lagrangian map for anisotropic synthetic turbulence: A priori tests," Phys. Fluids **26**, 075102 (2014).
[4] S.B. Pope, "Turbulent Flows," (Cambridge University Press, Cambridge, 2000).
[5] A. Juneja, D.P. Lathrop, K.R.Sreenivasan and G. Stolovitzky, "Synthetic turbulence," Phys. Rev. E **49**, 5179–5194 (1994).
[6] J.C.H. Fung, J.C.R. Hunt, N. A. Malik and R. J. Perkins, "Kinematic simulation of homogeneous turbulence by unsteady random Fourier modes," J. Fluid Mech. **236**, 281–318 (1992).
[7] N. Jarrin, S. Benhamadouche, D. Laurence, and R. Prosser, "A synthetic-eddy-method for generating inflow conditions for large-eddy simulations,"Int. J. Heat Fluid Flow **27**, 585593 (2006)
[8] N. Jarrin, R. Prosser, J.C. Uribe, S. Benhamadouche, and D. Laurence, "Reconstruction of turbulent fluctuations for hybrid RANS/LES simulations using a synthetic-eddy Method," Int. J. Heat Fluid Flow **30**, 435442 (2009).
[9] Y. Kim, I.P. Castro and Z.T. Xie, "Divergence-free turbulence inflow conditions for large-eddy simulations with incompressible flow solvers," Computers and Fluids **84**, 56–68 (2013).
[10] Z.T. Xie, and I. P. Castro, "Efficient generation of inflow conditions for large eddy simulation of street-scale flows," Flow, turbulence and combustion **81.3**, 449–470 (2008).
[11] B. de Laage de Meux, B. Audebert, R. Manceau, and R. Perrin, "Anisotropic linear forcing for synthetic turbulence generation in large eddy simulation and hybrid RANS/LES modelling," Phys. Fluids **27**, 035115 (2015).
[12] A. Rasam, G. Brethouwer, and A. Johansson, "An explicit algebraic model for the sub grid-scale passive scalar flux," J. Fluid Mech. **721**, 541 (2013).
[13] Y. Li, "The evolution towards the rod-like axisymmetric structure for turbulent stress tensor," Phys. Fluids **27**, 085104 (2015).
[14] C. Rosales, "Synthetic three-dimensional turbulent passive scalar fields via the minimal Lagrangian map," Phys. Fluids **23**, 075106 (2011).
[15] A. Pumir, "A numerical study of the mixing of a passive scalar in three dimensions in the presence of a mean gradient," Phys. Fluids **6**, 2118 (1994).
[16] B. Tao, J. Katz and C. Meneveau, "Statistical geometry of sub grid-scale stresses determined from holographic particle image velocimetry measurements," J. Fluid Mech. **457** (2002).
[17] B.I. Shraiman and E.D. Siggia, "Scalar turbulence," Nature **405**, 639 (2000).
[18] Z. Warhaft, "Passive scalars in turbulent flows,"Annu. Rev. Fluid Mech. **32**, 203 (2000).
[19] T. Vicsek and A. Barabasi, "Multi-affine model for the velocity distribution in fully turbulent flows," J. Phys. A **24**, L845 (1991).
[20] J. Eggers and S. Grossmanns, "Effect of dissipation fluctuations on anomalous velocity scaling in turbulence," Phys. Rev. A **45**, 2360 (1992).
[21] R. Benzi, L. Biferale, A. Crisanti, G. Paladin, M. Vergassola and A. Vulpiani, "A random process for the construction of multiaffine fields," Physica D **65**, 352 (1993).
[22] M. Holzer and D. Siggia, "Turbulent mixing of a passive scalar," Phys. Fluids **6**, 1820 (1994).
[23] R.H. Kraichnan, "Anomalous scaling of a randomly advected passive scalar," Phys. Rev. Lett. **72**, 1016 (1994).
[24] M. Chertov, G. Falkovich, I. Kolokolov, and V. Lebedev, "Normal and anomalous scaling of the fourth-order correlation function of a randomly advected passive scalar," Phys. Rev. E **52**, 4924 (1995).

[25]K. Gawedzki and A. Kupiainen, "Anomalous scaling of the passive scalar," Phys. Rev. Lett. **75**, 3834 (1995).
[26]U. Frisch, A. Mazzino, and M. Vergassola, "Intermittency in passive scalar advection," Phys. Rev. Lett. **80**, 5532 (1998).
[27]U. Piomelli, W. Cabot, P. Moin and S. Lee, "Sub-grid-scale backscatter in turbulent and transitional flows," Phys. Fluids A **3**, 1766 (1991).
[28]T. Watanabe and T. Gotoh, "Statistics of a passive scalar in homogeneous turbulence," New J. Phys. **6**, 40 (2004).
[29]C. Tong and Z. Warhaft, "On passive scalar derivative statistics in grid turbulence," Phys. Fluids **6**, 2165 (1994).
[30]L. Mydlarski and Z. Warhaft, "Passive scalar statistics in high-Peclet-number grid turbulence," J. Fluid Mech. **358**, 135 (1998).
[31]K.R. Sreenivasan and R. A. Antonia, "The phenomenology of small-scale turbulence," Annu. Rev. Fluid Mech. **29**, 435 (1997).
[32]B. Tao, J. Katz and C. Meneveau, "Geometry and scale relationships in high Reynolds number turbulence determined from three-dimensional holographic velocimetry," Phys. Fluids **12**, 941 (2000).
[33]K. Horiuti, "Roles of non-aligned eigenvectors of strain-rate and subgrid-scale stress tensors in turbulence generation," J. Fluid Mech. **491** (2003).
[34]S.G. Chumakov, "A priori study of subgrid-scale flux of a passive scalar in isotropic homogeneous turbulence," Phys. Rev. E **78**, 036313 (2008).
[35]C. Meneveau and J. Katz, "Scale-invariance and turbulence models for large-eddy simulation," Annu. Rev. Fluid Mech. **32**, 1 (2000).
[36]P.E. Dimotakis, "Turbulent mixing," Annu. Rev. Fluid Mech. **37**: 329-356 (2005).
[37]T. Gotoh and T. Watanabe, "Power and nonpower laws of passive scalar moments convected by isotropic turbulence," Phys. Rev. Lett. **115**, 114502 (2015).
[38]M.J. Beals, J.P. Fugal, R.A. Shaw, J. Lu, S.M. Spuler and J.L. Stith, "Holographic measurements of inhomogeneous cloud mixing at the centimeter scale," Science **350**, 6256 (2015).
[39]P. Flohr and J.C. Vassilicos, "A scalar subgrid model with flow structure for large-eddy simulations of scalar variances," J. Fluid Mech. **407**, 315–349 (2000).
[40]A. Scotti and C. Meneveau, "A fractal model for large eddy simulation of turbulent flow," Phys. D **127**, 198–232 (1999).
[41]D.R. Osborne, J.C. Vassilicos and J.D. Haigh, "One-particle two-time diffusion in three-dimensional homogeneous isotropic turbulence," Phys. Fluids **17**, 035104 (2005).
[42]F. Nicolleau and A. ElMaihy, "Effect of the Reynolds number on three and four-particle diffusion in three-dimensional turbulence using kinematic simulation," Phys. Rev. E **74**, 046302 (2006).
[43]H. Tennekes and J.L. Lumley, "A First course in turbulence," MIT Press Journals.
[44]L. Chevillard, E. Leveque, F. Taddia, C. Meneveau, H. Yu and C. Rosales, "Local and nonlocal pressure Hessian effects in real and synthetic fluid turbulence," Phys. Fluids **23**, 095108 (2011).
[45]P. Subedi, R. Chhiber, J. A. Tessein, M. Wan, and W. H. Matthaeus, "Generating synthetic magnetic field intermittency using a minimal multiscale Lagrangian mapping approach," The Astrophysical Journal **796**, 97 (2014).
[46]C. Nilsen and H. I. Andersson, "Mechanisms of particle clustering in Gaussian and non-Gaussian synthetic turbulence," Phys. Rev. E **90**, 043005 (2014).
[47]G.R. Tabor and M.H. Baba-Ahmadi, "Inlet conditions for large eddy simulation: A review," Computers and Fluids **39** , 553–567 (2010).
[48]A. Keating, U. Piomelli, E. Balaras and H.J. Kaltenbach, "A priori and a posteriori tests of inflow conditions for large-eddy simulation," Phys. Fluids **16**, 4696 (2004).
[49]L. Chevillard, R. Robert and V. Vargas, "A stochastic representation of the local structure of turbulence," Europhys. Lett. **89**, 54002 (2010).
[50]R.M. Pereira, C. Garban and L. Chevillard, "A dissipative random velocity field for fully developed fluid turbulence," J. Fluid Mech. **794**, 369 (2016).
[51]U. Frisch and J. Bec, "Burgulence," in New trends in turbulence Turbulence: nouveaux aspects by M. Lesieur, A. Yaglom and F. David (Ed.), 341–383 (2003).
[52]P. Sagaut, "Large eddy simulation for incompressible flows: an introduction," Springer Berlin Heidelberg (1998).
[53]T. Gotoh and T. Watanabe, "Scalar flux in a uniform mean scalar gradient in homogeneous isotropic steady turbulence," Physica D **241**, 141–148 (2012).
[54]J.A. Domaradzki and E.M. Saiki, "A subgrid-scale model based on the estimation of unresolved scales of turbulence," Phys. Fluids **9**, 2148 (1997).
[55]J. Bull and A. Jameson, "Explicit filtering and exact reconstruction of the sub-filter stresses in large eddy simulation," J. Comput. Phys. **306**, 117–136 (2016).
[56]N. Peters, "Turbulent combustion," Cambridge University Press (2000).
[57]H. Pitsch, "Large-eddy simulation of turbulent combustion," Ann. Rev. Fluid Mech. **38**, 453–82 (2006).
[58]G. Balarac, H. Pitsch, and V. Raman, "Development of a dynamic model for the subfilter scalar variance using the concept of optimal estimators, " Phys. Fluids **20**, 035114 (2008).
[59]G. Balarac, H. Pitsch, and V. Raman, "Modelling of the subfilter scalar dissipation rate using the concept of optimal estimators, " Phys. Fluids **20**, 091701 (2008).
[60]E. Knudsen, E. S. Richardson, E. M. Doran, H. Pitsch, and J. H. Chen, "Modelling scalar dissipation and scalar variance in large eddy simulation: Algebraic and transport equation closures," Phys. Fluids **24**, 055103 (2012).
[61]Y. Gao, N. Chabraborty, and N. Swaminathan, "Dynamic closure of scalar dissipation rate for large eddy simulations of turbulent premixed combustion: a direct numerical simulations analysis," Flow Turbulence Combust **95**, 775–802 (2015).
[62]L. S. G. Kovasznay, "Spectrum of locally isotropic turbulence, " Journal of the Aeronautical Sciences **15**, 745–753 (1948).
[63]S. Panchev, "Kovasznay's spectral theory of turbulence," Phys. Fluids **12**, 935(1969).
[64]F. Porte-Agel, C. Meneveau, and M. B. Parlange, "A scale-dependent dynamic model for large-eddy simulation: application to a neutral atmospheric boundary layer," J. Fluid Mech. **415**, 261–284 (2000).